

Flexing into motion: A locomotion mechanism for soft robots



Xuance Zhou^{a,2}, Carmel Majidi^{b,1}, Oliver M. O'Reilly^{a,*,2}

^a Department of Mechanical Engineering, University of California at Berkeley, Berkeley CA 94720-1740, USA

^b Department of Mechanical Engineering, Carnegie Mellon University, Pittsburgh PA 15213, USA

ARTICLE INFO

Article history:

Received 15 September 2014

Received in revised form

20 January 2015

Accepted 3 March 2015

Available online 31 March 2015

Keywords:

Adhesion

Stick-slip friction

Peristaltic locomotion

Soft robot

Rod theory

Stability

ABSTRACT

Several recent designs of soft robots feature locomotion mechanisms that entail orchestrating changes to intrinsic curvature to enable the robot's limbs to either stick, adhere, or slip on the robot's workspace. The resulting locomotion mechanism has several features in common with peristaltic locomotion that can be found in the animal world. The purpose of the present paper is to examine the feasibility of, and design guidelines for, a locomotion mechanism that exploits the control of intrinsic curvature on a rough surface. With the help of a quasi-static analysis of a continuous model of a soft robot's limb, we show precisely how locomotion is induced and how the performance can be enhanced by controlling the curvature profile. Our work provides a framework for the theoretical analysis of the locomotion of the soft robot and the resulting analysis is also used to develop some design guidelines.

© 2015 Elsevier Ltd. All rights reserved.

1. Introduction

The soft robot's unique promise for enabling inherently safe and adaptive features has made it one of the most appealing emerging fields in robotics. Recent advancements in the field of soft robots includes the development of bodyware control and engineered adhesive materials (see, e.g., [2,4,5] and the three examples shown in Fig. 1). For some soft robot designs, such as the quadruped shown in Fig. 1(a) from [1], locomotion is achieved by using the coordinated interaction of four soft limbs with the external surface. Each of the limbs in this design contain a set of pneumatic actuators which change the intrinsic curvature and flexural rigidity of the limb [6].

Other notable examples of locomoting soft robots include worm- or snake-like designs where serpentine locomotion is enabled by using either a traveling wave generated by a fluidic elastomer actuator [3], or hydraulic pressure [7] or shape memory alloys [8]. These designs are similar to those featuring in the so-called continuum or serpentine robots which feature in surgical and industrial applications [9]. As discussed in [10], similar locomotion mechanisms can be found in certain other robots such as the ETH-Zürich MagMite [11,12], the University of Texas at Arlington ARRIpede robot [13,14], a design from the University of Trento [15,16] and a design from Carnegie-Mellon University [17] that features an electromagnetic drive. The designs

listed above that feature varying curvature and adhesion of limbs also have their natural counterparts in a wide variety of creatures who move using limbless crawling (peristaltic locomotion [18–20]). In these animals, varying curvature is realized by muscles and adhesion is achieved either by the use of bristles or mucus [21].

The wealth of designs and implementations in the aforementioned works make it difficult to gain a perspective on how locomotion can be induced by properly coordinating the interaction of the limbs with the ground plane on which the robot moves. In order to examine this issue, a rod-based, flexible model for a limb which is attached to a mass m is developed and examined. Referring to Fig. 2, we consider a block of mass m that is free to move on a rough horizontal surface. The block is attached to a flexible rod whose intrinsic curvature κ_0 is assumed to be controllable. By varying the profile $\kappa_0(s)$ of the intrinsic curvature, the contact between the rod and the ground can be changed. In particular, we seek to examine the best profiles $\kappa_0(s)$ which enable a locomotion of the block such as that shown in Fig. 3.

While the majority of works in the application area of interest have addressed hardware design and fabrication, less attention has been devoted to a numerical analysis of relevant theoretical models. Such analyses are challenging because the behavior is often governed by non-linear PDEs and recourse to numerical methods is typical. The present paper provides a systematic analysis of the feasibility of a locomotion scheme using a quasi-static analysis. While we do not specify on the precise mechanism by which the intrinsic curvature is changed, there has been an increased interest in the development of mechanisms for changing κ_0 in components of soft robots. The interested reader is referred to [22–26] for examples of these mechanisms.

* Corresponding author.

E-mail address: oreilly@berkeley.edu (O.M. O'Reilly).

¹ Tel.: +1 412 268 2492; fax: +1 412 268 3348.

² Tel.: +1 510 642 0877; fax: +1 510 643 5599.

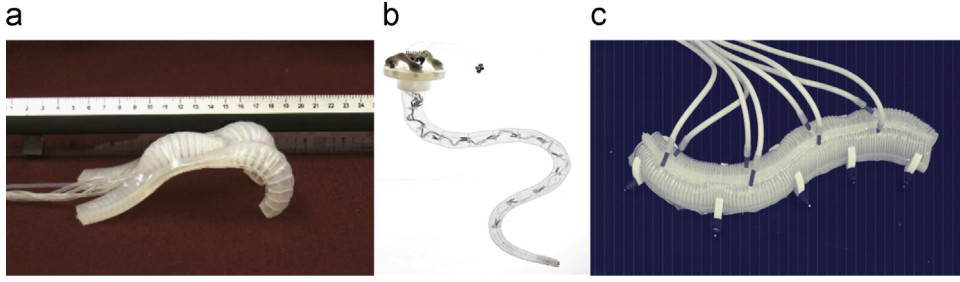


Fig. 1. Examples of soft robots. (a) Quadruped with inflatable bending actuators from [1]. (b) Octopus-like soft robot from [2], and (c) soft robot with fluidic elastomer actuator from [3].

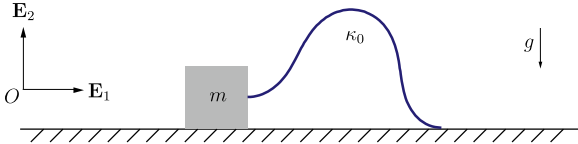


Fig. 2. Schematic of a rod-based model for the soft robot. One end of the rod is attached to a mass m .

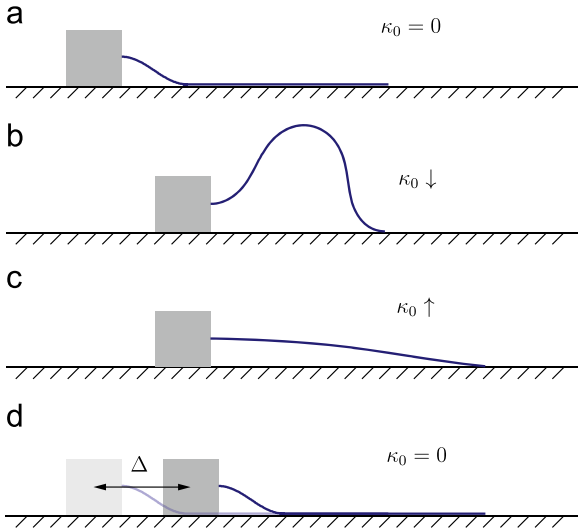


Fig. 3. Illustration of the locomotion for the model system shown in Fig. 2. In (a) the system is at rest and the soft limb is attached to the ground, then in (b) the profile $\kappa_0(s)$ of the intrinsic curvature changes and the block attached to the soft limb moves forward. In (c), the intrinsic curvature is relaxed, the block sticks to the ground, and the tip of the soft limb slips forward. In (d), the soft limb in contact with the ground plane forms a dry-adhesive bond with the plane and a single cycle of the locomotion mechanism is complete. The net displacement Δ for a single cycle is also shown.

The paper is organized as follows: in the next section, Section 2, a model for the system shown in Figs. 2 and 3 is established using rod theory and the governing equations for the two configurations shown in Fig. 3 are derived using variational principles. We follow [27,28] in the treatment of stability criteria for the dry adhesion of rods. In Section 3, numerical integrations of the governing equations are analyzed. Furthermore, the stability of these solutions is discussed in Section 4. Our analyses demonstrate how controlling the intrinsic curvature can coordinate the interaction between the soft robot and ground plane in a manner that leads to effective locomotion of the system. We conclude the paper with a discussion on different curvature profiles in Section 5 and a set of design recommendations for optimal performance of soft robot featuring varying curvature and adhesion.

2. A simple model for a soft-limbed robot

We are interested in developing a simple model to analyze the salient features for the locomotion of a soft robot. Referring to

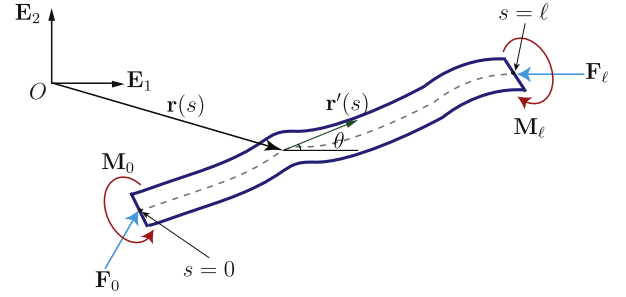


Fig. 4. Schematic of a flexible elastic rod which is subject to a terminal force \mathbf{F}_0 and terminal moment \mathbf{M}_0 at $s=0$ and a terminal force \mathbf{F}_ℓ and terminal moment \mathbf{M}_ℓ at the end $s=\ell$. The coordinate s parameterizes the centerline of the rod.

Fig. 2, the model has two components: a rigid mass and a heavy flexible elastic component. Thus one approach to modeling the robot is to use Euler's theory of an elastic rod which is known as an elastica. Euler's theory can be readily modified to include varying intrinsic curvature and terminal loads due to added mass or friction forces. Our developments and notation closely follow our earlier works [27,28] on adhered intrinsically curved rods.

2.1. Background

The rod is modeled using Euler's theory of an elastica as a uniform rod of length ℓ which has a flexural rigidity EI , mass per unit length ρ and an externally controlled intrinsic curvature κ_0 . As discussed in [6], the pneumatic actuation system in some soft robots induces changes to EI and ρ but we do not consider these effects here. Incorporating them into the model would follow the lines of similar developments in models for growing plant stems that are discussed in [29,30]. We also note that the rod is assumed to be inextensible and unshearable. Adding these two kinematic features would entail using a more elaborate rod theory.

Referring to Fig. 4, the arc length of the centerline of the rod is parameterized using a coordinate $s \in [0, \ell]$. The position vector of a material point at $s=s_1$ on the centerline of the rod has the representation

$$\mathbf{r}(s=s_1) = X(s=s_1)\mathbf{E}_1 + Y(s=s_1)\mathbf{E}_2, \quad (1)$$

where the Cartesian coordinates X and Y are defined by

$$\begin{aligned} X(s=s_1) &= X(s=0) + \int_0^{s_1} \cos(\theta(\xi)) d\xi, \\ Y(s=s_1) &= Y(s=0) + \int_0^{s_1} \sin(\theta(\xi)) d\xi. \end{aligned} \quad (2)$$

In (2), the angle θ is defined as the angle that the unit tangent vector \mathbf{r}' makes with the horizontal \mathbf{E}_1 direction

$$\mathbf{r}' = \cos(\theta(s))\mathbf{E}_1 + \sin(\theta(s))\mathbf{E}_2 \quad (3)$$

where the prime denotes the partial derivative with respect to s .

In addition to a gravitational force per unit mass $-\rho g \mathbf{E}_2$ and an adhesive potential energy Ω on certain segments of the rod's

lateral surface, a terminal force \mathbf{F}_ℓ and terminal moment \mathbf{M}_ℓ are presumed to act at the tip $s = \ell$. In the problem at hand, the terminal loading will be used to model the contact conditions at the end of the soft limb. The bending moment \mathbf{M} in the rod is prescribed by a classic constitutive equation

$$\mathbf{M} = EI(\theta' - \kappa_0)\mathbf{E}_3 \quad (4)$$

where κ_0 is a signed intrinsic curvature.

Along the length of the rod, discontinuities typically occur and it is necessary to define the following limits for any function $\mathcal{X} = \mathcal{X}(s, \theta(s), \theta'(s))$:

$$\begin{aligned} \mathcal{X}(\zeta^-) &= \lim_{s \nearrow \zeta} \mathcal{X}(s, \theta(s), \theta'(s)), \\ \mathcal{X}(\zeta^+) &= \lim_{s \searrow \zeta} \mathcal{X}(s, \theta(s), \theta'(s)). \end{aligned} \quad (5)$$

The jump or discontinuity in the function \mathcal{X} at the point $s = \zeta$ can then be represented using a compact notation:

$$[[\mathcal{X}]]_\zeta = \mathcal{X}(\zeta^+) - \mathcal{X}(\zeta^-). \quad (6)$$

We shall assume that \mathbf{r} is continuous (i.e., there are no breaks in the rod). It follows that θ will then be continuous and $[[\mathbf{r}']]_\zeta = \mathbf{0}$ for all $\zeta \in [0, \ell]$.

Henceforth we develop models for two distinct configurations of the rod. In the first configuration, which is shown in Figs. 3(c) and 5, the end of the rod at $s = \ell$ is in point contact with the ground plane. We refer to this configuration as State I. The second configuration of interest, which we refer to as State II, arises when a portion of the rod $s \in [\gamma, \ell]$ is in contact with the ground plane and a dry adhesion is present at this interface. Examples of this configuration can be seen in Figs. 3(a, b, and d) and 6. We now turn towards establishing the governing equations for the models for States I and II.

2.2. Governing equations for State I

In State I, the mass m is assumed to be held stationary with the help of static friction. We define the end point of the rod that connects to the singular mass to be $s = 0$ and the tip of the rod that touches the rough ground to be $s = \ell$. The normal force acting on m is denoted by $N_2\mathbf{E}_2$ and $F_{f_2}\mathbf{E}_1$ denotes the friction force. At the tip of the rod, a normal force $N_1\mathbf{E}_2$ and a friction force $F_{f_1}\mathbf{E}_1$ are assumed to act. The normal force $N_1\mathbf{E}_2$ is a constraint force due to the unilateral constraint

$$\int_0^\ell \sin(\theta(s)) ds = -h. \quad (7)$$

Here, $h = Y(0) - Y(\ell)$ is a constant height.

For our quasi-static analysis, where the inertias of the mass and rod are ignored, there are two cases to consider. In the first case the tip of the rod is assumed to be stationary. Thus, the static friction force $F_{f_1}\mathbf{E}_1$ in this case is a constraint force due to the

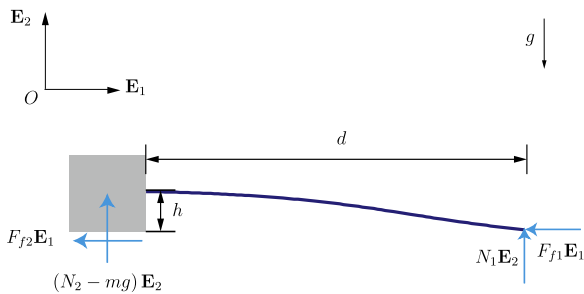


Fig. 5. Free body diagram for the model for State I. In this model, point contact at the tip of the rod $s = \ell$ and the ground plane is assumed. The mass m is assumed to be held stationary by static friction.

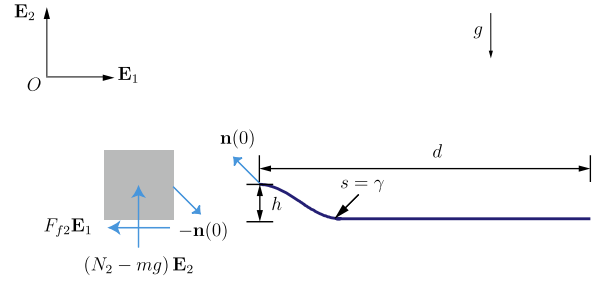


Fig. 6. Free body diagram for the model for State II. In this model, a portion $\ell - \gamma$ of the rod adheres to the ground plane.

constraint

$$\int_0^\ell \cos(\theta(s)) ds = d. \quad (8)$$

Here, $d = X(\ell) - X(0)$ is a constant. With the help of the static friction criterion and assuming the same coefficient of static friction μ_s between the mass m and the ground and the rod tip and the ground, we find that

$$\begin{aligned} N_2 &= mg + \rho g \ell - N_1, \\ F_{f_1} &= F_{f_2}, \end{aligned} \quad (9)$$

where the normal and friction forces satisfy the following criteria:

$$\begin{aligned} |F_{f_1}| &\leq \mu_s N_1, \quad N_1 > 0, \\ |F_{f_2}| &\leq \mu_s N_2, \quad N_2 > 0. \end{aligned} \quad (10)$$

Once the inequality in (10)₁ is violated, the static friction force at the tip of the rod changes to dynamic friction and d no longer remains constant. In this case, (10)₁ is replaced with

$$F_{f_1} = -\mu_d N_1 \frac{\dot{X}(\ell)}{|\dot{X}(\ell)|}. \quad (11)$$

For present purposes, we are particularly interested in changing the curvature profile $\kappa_0(s)$ so that $\frac{\dot{X}(\ell)}{|\dot{X}(\ell)|} = 1$ and the tip of the rod moves forward.

Because, the mass m is assumed to be fixed in State 1, the potential energy of the rod consists of the sum of the strain energy, gravitational potential energy and the potential energy of the terminal load \mathbf{F}_ℓ

$$V = \int_0^\ell \left\{ \frac{EI}{2} (\theta' - \kappa_0)^2 + \rho g Y(s) - \mathbf{F}_\ell \cdot \mathbf{r} \right\} ds, \quad (12)$$

where

$$Y(s) = \int_0^s \sin(\theta(\xi)) d\xi, \quad \mathbf{F}_\ell = F_{f_1}\mathbf{E}_1 + N_1\mathbf{E}_2. \quad (13)$$

The integral can be simplified using a standard change in the order of integration (see [31] for a clear discussion)

$$\int_0^\ell \rho g \int_0^s \sin(\theta(\xi)) d\xi ds = \int_0^\ell \rho g (\ell - s) \sin(\theta(s)) ds. \quad (14)$$

Since we are assuming that both ends of the rod are fixed, the first variation of V can be used to derive the boundary-value problem for the deformed shape θ of the rod:

$$EI(\theta'' - \kappa_0') - \rho g(\ell - s) \cos(\theta) + N_1 \cos(\theta) - F_{f_1} \sin(\theta) = 0, \quad s \in [0, \ell]. \quad (15)$$

In addition, the sought-after solution $\theta(s)$ to (15) needs to satisfy the boundary conditions

$$\begin{aligned} \theta(0) &= 0, \quad \theta'(\ell) = \kappa_0(\ell), \\ \int_0^\ell \cos(\theta(s)) ds &= d, \quad \int_0^\ell \sin(\theta(s)) ds = -h, \end{aligned} \quad (16)$$

and also satisfy (10). If the static friction criterion (10)₁ is violated then the tip of the rod will slip and the friction force at the tip becomes dynamic (11). In this case, we need to solve (15) for θ subject to the boundary conditions

$$\theta(0) = 0, \quad \theta'(\ell) = \kappa_0(\ell), \quad \int_0^\ell \sin(\theta(s)) ds = -h. \quad (17)$$

That is, the constraint (8) no longer holds.

2.3. Governing equations for State II

In State II, a portion of the rod from $s = \gamma$ to $s = \ell$ is assumed to be in continuous contact with the ground plane. At the point $s = 0$ where the rod is clamped to the mass m , the rod exerts a contact force $-\mathbf{n}(0)$ on m . Using a balance of linear momentum for m and ignoring the inertia of m and the rod, we find that

$$\mathbf{n}(0) = n_1(0)\mathbf{E}_1 + n_2(0)\mathbf{E}_2 = N_2\mathbf{E}_2 - mg\mathbf{E}_2 + F_{f_2}\mathbf{E}_1. \quad (18)$$

As with the model for State I, N_2 and F_{f_2} are the normal and friction forces, respectively, acting on m .

With the help of the static friction criterion, it is straightforward to see the following conditions need to be satisfied if the mass m is to remain stationary:

$$n_2 \geq -mg, \quad |n_1| \leq \mu_s(n_2(0) + mg). \quad (19)$$

If the mass m were to slip, then ignoring the inertias of the rod and mass m , we find that (19) needs to be replaced with

$$n_2 \geq -mg, \quad n_1 = -\mu_k(n_2(0) + mg) \frac{\dot{X}(0)}{|\dot{X}(0)|}. \quad (20)$$

To find the terminal force $\mathbf{n}(\gamma)$, we use a local form of the balance of linear momentum for the rod:

$$\mathbf{n}' + \rho\mathbf{f} = 0. \quad (21)$$

For the detached segment $s \in [0, \gamma]$ of the rod, $\mathbf{f} = -g\mathbf{E}_2$, and so we find that

$$n_1(\gamma) = n_1(0), \quad n_2(\gamma) = n_2(0) - \rho g(\ell - \gamma). \quad (22)$$

The results (19), (20) and (22) will be used to compute the potential energy of the rod.

The total energy of the rod in State II consists of the sum of the strain energy, gravitational potential energy, the potential energy due to the terminal load, and the adhesion energy. Here, we follow the treatment in [27,28] and model the adhesion energy using a constant ω for the adhesion energy per unit length along the adhered part $s \in [\gamma, \ell]$. It is straightforward to show that the potential energy of the rod is

$$V = \int_0^\gamma \left\{ \frac{EI}{2} (\theta' - \kappa_0)^2 + \rho g Y(s) - \mathbf{n}(\gamma) \cdot \mathbf{r}' \right\} ds$$

$$+ \int_\gamma^\ell \left\{ \frac{EI}{2} (\theta' - \kappa_0)^2 + \rho g h - \mathbf{n}(0) \cdot \mathbf{r}' + \omega \right\} ds, \quad (23)$$

where

$$Y(s) = \int_0^s \sin(\theta(\xi)) d\xi. \quad (24)$$

In establishing (23) we emphasize that we are ignoring inertial effects.

Similar to State I, the first variation of V can be performed to establish the boundary-value problem which is used to determine the deformed shape θ for the detached part of the rod:

$$EI(\theta'' - \kappa_0') - \rho g(\gamma - s) \cos(\theta) + n_2(\gamma) \cos(\theta) - n_1(\gamma) \sin(\theta) = 0, \quad s \in [0, \gamma]. \quad (25)$$

If (25) features static friction, then θ must satisfy the boundary conditions

$$\theta(0) = 0, \quad \theta(\gamma) = 0, \quad \left[\frac{EI}{2} (\theta' - \kappa_0)^2 - \mathbf{n} \cdot \mathbf{r}' \right]_\gamma = \omega, \quad \int_0^\ell \cos(\theta(s)) ds = d, \quad \int_0^\ell \sin(\theta(s)) ds = -h \quad (26)$$

and (19). Alternatively, if m is in motion, then θ must satisfy the boundary conditions

$$\theta(0) = 0, \quad \theta(\gamma) = 0, \quad \left[\frac{EI}{2} (\theta' - \kappa_0)^2 - \mathbf{n} \cdot \mathbf{r}' \right]_\gamma = \omega, \quad \int_\gamma^\ell \sin(\theta(s)) ds = -h \quad (27)$$

and (20).

3. The locomotion mechanism

To discuss the locomotion mechanism shown in Fig. 3, it is convenient to divide the mechanism into a series of phases as follows:

- (A) In Phase A, the mass m is fixed and tip of the rod is initially stationary and in contact with the ground plane. By judiciously varying the curvature profile $\kappa_0(s)$, the tip of the rod is induced to slip as far forward as possible.
- (B) In Phase B, the mass m is fixed and, again by carefully varying $\kappa_0(s)$, the length of the rod in contact with the ground plane is increased using dry adhesion.
- (C) In Phase C, the adhered length of the lateral surface of the rod is decreased by varying $\kappa_0(s)$ (i.e., peeling occurs), the mass m slips, and is promoted to move as far forward as possible.

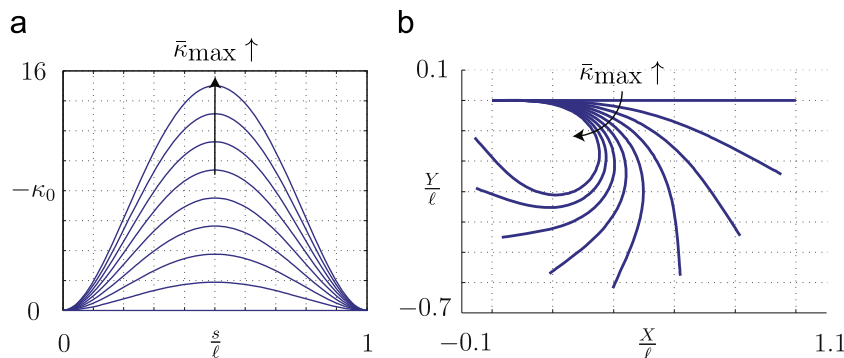


Fig. 7. Features of the curvature profile (28) as the parameter $\bar{\kappa}_{\max}$ is varied. (a) The dimensionless curvature throughout the deformed rod. (b) The corresponding deformed shape of a heavy rod with an intrinsic curvature profile (28) and a vertical gravity loading. One end of the rod is assumed to be clamped while the other is free. The dimensionless flexural rigidity D of the rod is $D = \frac{EI}{\rho g \ell^3} = 0.1$.

At the end of Phase C, the only portion of the lateral surface of the rod that is in contact with the ground plane is the tip of the rod. For the mass to move further, Phases A, B, and C are repeated sequentially. We now turn to examining the three phases in turn.

3.1. Curvature profile and dimensionless parameters

In our work, slip, adhesion, and peeling are controlled by varying the intrinsic curvature profile and the choice of this profile is critical to the feasibility of the proposed locomotion mechanism. For the purposes of discussion, it is convenient to choose a particular curvature profile which we express using a dimensionless profile $\bar{\kappa}_0$

$$\bar{\kappa}_0 = \frac{\kappa_0}{\ell} = -16\bar{\kappa}_{\max}\bar{s}^2(1-\bar{s})^2, \quad (28)$$

where $\bar{\kappa}_{\max}$ is a constant and the dimensionless arc length \bar{s} is defined as

$$\bar{s} = \frac{s}{\ell}. \quad (29)$$

The behavior of a clamped-free rod loaded by its own weight and endowed with the curvature profile (28) is shown in Fig. 7. This figure shows that the curvature profile does not generate physically unrealistic self-intersections of the rod as $\bar{\kappa}_{\max}$ is varied.

Numerical simulations in the sequel are performed using Matlab's bvp4c package. For these simulations, it is convenient to define a dimensionless flexural rigidity D , mass M , and adhesion energy W_{ad}

$$D = \frac{EI}{\rho g \ell^3}, \quad M = \frac{m}{\rho \ell}, \quad W_{\text{ad}} = \frac{\omega}{\rho g \ell}. \quad (30)$$

We also use the weight $\rho g \ell$ of the rod to non-dimensionalize the friction and normal forces. In an effort to make our figures more concise, we denote sticking of the mass m by “S”, a tendency of the mass to move to the left by “L” and a tendency to move to the right by “R”.

3.2. Phase A

We start by considering the tip of the rod in point contact with the ground plane as shown in Fig. 8. A key to successful locomotion is to vary the normal force N_1 at the contact point so that the static friction criterion will be violated and the tip of the rod will slip forward. To see how this can be achieved using the profile (28), we solve the boundary value problem given by (15) and (16) to determine the deformed shape of the rod and the dimensionless normal $\frac{N_1}{\rho g \ell}$ and friction $\frac{F_{f1}}{\rho g \ell}$ forces at the tip.

As can be seen from Fig. 8(b), as $\bar{\kappa}_{\max}$ decreases, eventually a point is reached where the tip of the rod slips. For the example shown, this critical point occurs when $\bar{\kappa}_{\max} < 6.03$. For the given

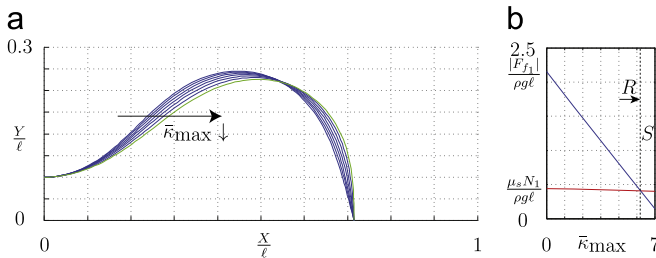


Fig. 8. The first stage of Phase A of the locomotion scheme where the static friction acts at the tip of the rod. (a) The deformed shape of the rod as $\bar{\kappa}_{\max}$ decreases from 7 to 0. (b) The corresponding dimensionless friction $\frac{|F_{f1}|}{\rho g \ell}$ and (scaled) normal $\frac{\mu_s N_1}{\rho g \ell}$ forces acting at the tip of the rod in contact with the ground plane. For the results shown, $d=0.72$, $D=\frac{EI}{\rho g \ell^3}=0.1$, and $\mu_s=0.3$. When $\bar{\kappa}_{\max} < 6.03$, the static friction criterion is violated and so one of the configurations shown in (a) is not realizable.

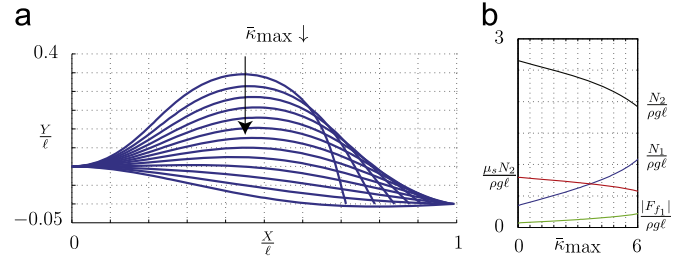


Fig. 9. The second stage of Phase A of the locomotion scheme where the tip of the rod is slipping forward. (a) The shape of the rod as $\bar{\kappa}_{\max}$ varies. (b) The corresponding dimensionless forces acting at both ends of the rod. For the problem at hand, $F_{f1} = -F_{f2}$ so the mass m remains stationary. For the results shown, $D=\frac{EI}{\rho g \ell^3}=0.1$, $\mu_k=0.2$, $\mu_s=0.3$, $M=\frac{m}{\rho \ell}=2$, and $\bar{\kappa}_{\max}$ ranges from 6 to 0.

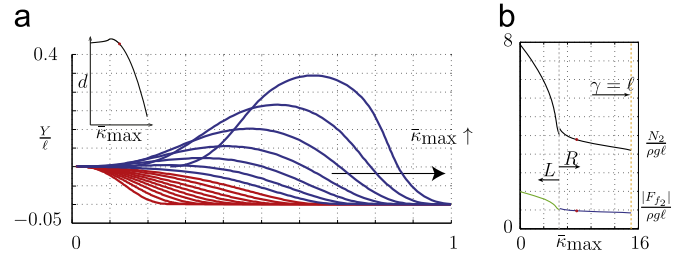


Fig. 10. Phase C of the locomotion scheme where the adhered length of the rod is decreasing and the mass m is in motion. (a) The shape of the rod as $\bar{\kappa}_{\max}$ varies. (b) The corresponding dimensionless forces acting at the mass m . For the results shown, $W_{\text{ad}}=\frac{\omega}{\rho g \ell}=3.2$, $M=\frac{m}{\rho \ell}=2$, $D=\frac{EI}{\rho g \ell^3}=0.1$, $\mu_k=0.2$ and $\bar{\kappa}_{\max}$ increases from 0 to 15.

$\kappa_0(s)$, the tip slips to the right. Once the slipping is about to occur, the friction force at the tip changes to dynamic friction and we need to reformulate the boundary value problem in order to determine the deformed shape of the rod. The resulting reformulated boundary value problem now features (15) and (17). As $\bar{\kappa}_{\max}$ is decreased from the critical value 6.03 to 0, we observe from Fig. 9(a) that the tip moves increasingly forward and the length $\frac{d}{\ell} \rightarrow 1$. The resulting solution for various values of $\bar{\kappa}_{\max}$ is shown in Fig. 9(a).

During Phase A of the locomotion scheme, it is important that the mass m remains stationary while the tip of the rod slips. To see if m remains at rest, we need to verify the static friction criterion for m . As can be seen from the graphs for $\mu_s \frac{N_2}{\rho g \ell}$ and $\frac{|F_{f1} - F_{f2}|}{\rho g \ell}$ in Fig. 9(b), the static friction criterion holds as $\bar{\kappa}_{\max}$ is decreased from 6 to 0.

3.3. Phase B

At the end of Phase A, the tip of the rod has extended as far to the right as possible and $\bar{\kappa}_{\max} = 0$. It is at this stage that we assume that dry adhesion is present between the lateral surface of the rod and the ground plane. Our simulations also show the expected results that more flexible (EI is small) heavier ($\rho \ell$ is large) rods are conducive to having a large contact length. It is straightforward to solve the resulting boundary value problem for Phase B in order to determine the adhered length of the rod and so we now turn to Phase C.

3.4. Phase C

At the start of Phase C, the curvature parameter $\bar{\kappa}_{\max} = 0$. Referring to Fig. 10(a), as $\bar{\kappa}_{\max}$ increases from 0, the rod peels from the surface. We observe from the inset image in Fig. 10(a) of d as a function of $\bar{\kappa}_{\max}$ that the mass m moves initially to the left (d increases), but eventually, the mass m moves to the right and the

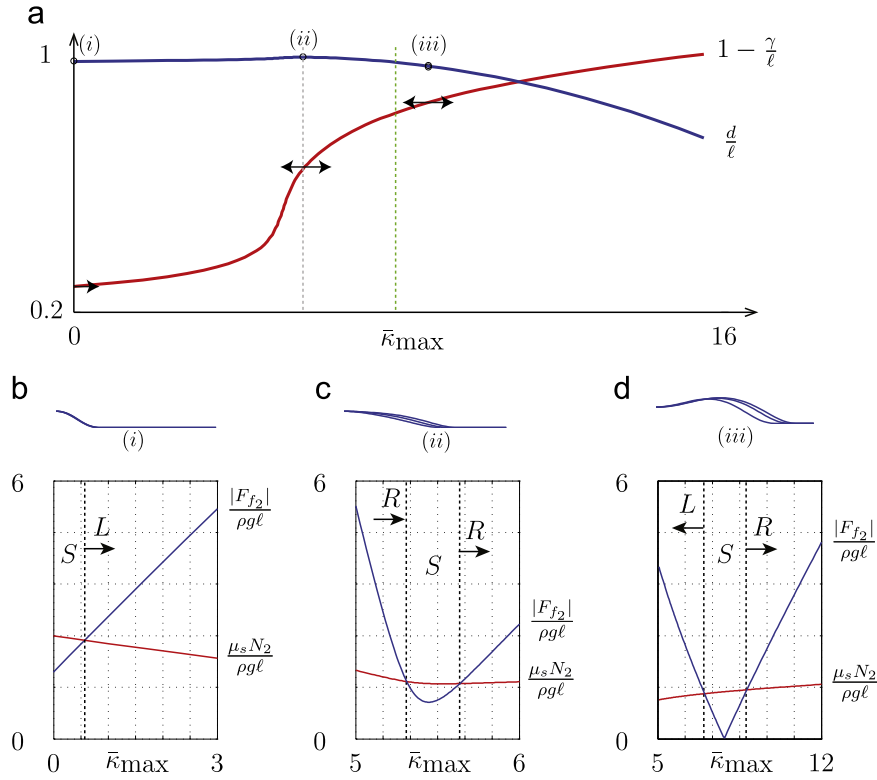


Fig. 11. Illustration of Phase C of the locomotion scheme featuring State II where static friction acting on the mass m is overcome and motion of m is achieved. In (a) the dimensionless length of the rod $\frac{d}{l}$ and the dimensionless detached length $1 - \frac{\gamma}{l}$ as $\bar{\kappa}_{\max}$ varies when the mass m slips. (b) The corresponding dimensionless forces acting at the singular mass for fixed d and γ for three representative regimes: (b) $\bar{\kappa}_{\max} \in [0, 3]$; (c) $\bar{\kappa}_{\max} \in [5, 6]$; and (d) $\bar{\kappa}_{\max} \in [5, 12]$. For the results shown $W_{ad} = \frac{\omega}{\rho g \ell} = 3.2$, $M = \frac{m}{\rho \ell} = 2$, $D = \frac{EI}{\rho g \ell^3} = 0.1$, $\mu_k = 0.2$, $\mu_s = 0.3$ and $\bar{\kappa}_{\max}$ ranges from 0 to 15. The inset images show the deformed state of the rod.

desired locomotion is achieved. In order to switch from State II to State I, we need to make γ reach ℓ . As illustrated in Fig. 10(a), as $\bar{\kappa}_{\max}$ increases, γ will eventually reach ℓ with $\bar{\kappa}_{\max} = 15$. At this stage in the locomotion process, only the tip of the rod at $s = \ell$ is in contact with the ground plane.

The reason for the initial increase in d can be explained by noting that as we started increasing $\bar{\kappa}_{\max}$, the rod peeled but $\theta'(\gamma)$ decreased. In order to accommodate the decreased value of $\theta'(\gamma)$, d was forced to increase. However, as $\bar{\kappa}_{\max}$ is increased beyond ≈ 5.42 in Fig. 10, d will start to decrease and the mass will move forward. In our simulations of the boundary value problem to analyze this case we updated the value of $\frac{\dot{X}(0)}{|\dot{X}(0)|}$ to accommodate the cases where d was decreasing and increasing.

A potential realization of the locomotion induced by Phase C is shown in Fig. 11(a). The dimensionless plots of d and $\ell - \gamma$ as a function of $\bar{\kappa}_{\max}$ shown in this figure were constructed by quasi-statically increasing the latter variable from 0 and examining the detachment of the rod and the movement of the mass m .

It is of great interest to examine the robustness of the locomotion during Phase C to perturbations in the changes in system parameters such as μ_k . To this end, we examined three distinct instances, labelled $i - iii$ on the graph in Fig. 11(a). For a given d , we are interested in how varying $\bar{\kappa}_{\max}$ can produce changes in the friction force F_{f_2} and normal force N_2 acting on the mass m .³ Consider for instance, the point i . As shown in Fig. 11(b), if we vary $\bar{\kappa}_{\max}$ while assuming that d is constant, then we find that eventually the mass will slip to the left. On the other hand for ii , as shown in Fig. 11(c), we find that varying $\bar{\kappa}_{\max}$ will induce the mass to move to the right. This is in contrast to iii (cf. Fig. 11(d)),

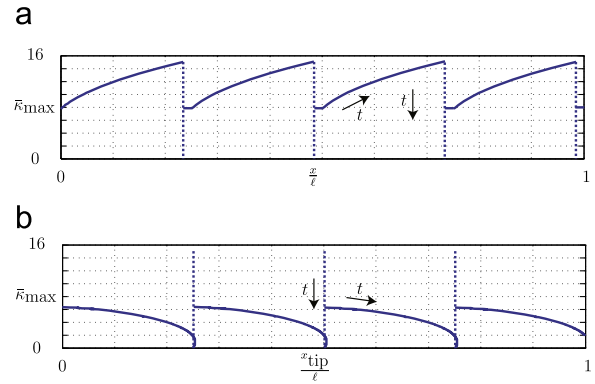


Fig. 12. Results from the quasi-static analysis of the (a) change x in the mass m 's position in the E_1 direction and (b) change x_{tip} in the tip of the rod's position in the E_1 direction under the excitation of a periodic $\bar{\kappa}_{\max}$. In (a), $\bar{\kappa}_{\max}$ ranges from 7.65 to 15.0 and in (b) $\bar{\kappa}_{\max}$ ranges from 0 to 6.56. The dimensionless parameters for this model are $W_{ad} = \frac{\omega}{\rho g \ell} = 3.2$, $M = \frac{m}{\rho \ell} = 2$, $D = \frac{EI}{\rho g \ell^3} = 0.1$, $\mu_k = 0.2$, and $\mu_s = 0.3$.

where varying $\bar{\kappa}_{\max}$ is capable of inducing the mass to move to the left or the right. The nature of the variations in F_{f_2} and N_2 with $\bar{\kappa}_{\max}$ implies that the locomotion scheme is robust with respect to small changes in μ_s and μ_k .

3.5. The locomotion cycle

We now summarize our findings by illustrating the locomotion of the mass m that can be achieved by cyclically varying $\bar{\kappa}_{\max}$ from $0 \rightarrow 15$. As can be seen in Fig. 12, where the dimensionless displacement $\frac{x}{l}$ of the center of mass is displayed, the mass m will initial move backwards, but as $\bar{\kappa}_{\max}$ is increased further, the mass will move forward.

³ The change in $\bar{\kappa}_{\max}$ will induce changes to γ .

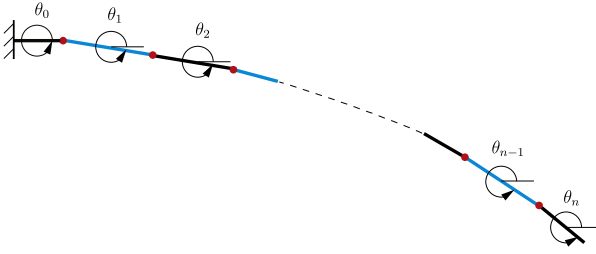


Fig. 13. Schematic of the discretization scheme for the rod.

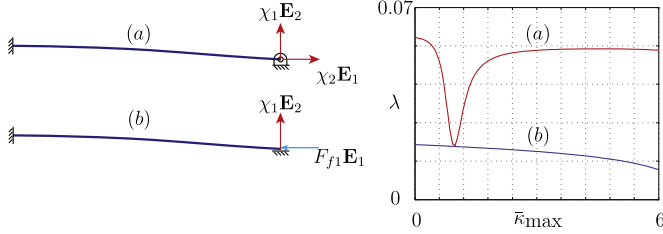


Fig. 14. Verification of the stability of the equilibrium configuration shown in Fig. 9 by examining the smallest eigenvalue λ of $E^T LE$: (a) corresponds to the case when the static friction force is modeled as a constraint in the E_1 direction; and (b) corresponds to the case when the static friction force at the tip of the rod is approximated by a constant force. For the examples shown, $D = \frac{EI}{\rho g \ell^3} = 0.1$, $\mu_k = 0.2$, $M = \frac{m}{\rho \ell} = 2$ and $\bar{\kappa}_{\max}$ ranges from 0 to 6.

4. Stability analysis

The equilibrium configurations of the rod discussed in Section 3 feature large deformations and must be stable in order for the locomotion scheme to be realized. The presence of friction considerably complicates an analysis of this stability and we are forced in the sequel to perform an approximate stability analysis. Thus, for the configurations referred to as State I, we analyze stability when the friction forces are static by considering the two limiting cases of assuming that a constant force acts at the rod tip and the tip is fixed (so the rod is clamped–fixed). The approximations we adopt for examining the stability of State II are to assume that the mass m is fixed. In this case, we can use the recently developed stability criteria for elastic rods with dry adhesion that can be found in [27,28].

4.1. Stability analysis for State 1

In order to cope with the challenge brought up by isoperimetric constraint and friction in the stability analysis of State I, we discretize the rod into a series of elements and approximate the friction in two separate manners. First, we model the friction as a constraint and second we approximate the friction as a constant force. Next, the rod is modeled as a set of $n-1$ segments of length ds and 2 segments of length $\frac{ds}{2}$ with $nds = \ell$, the friction force at the tip is treated as a constraint (cf. Figs. 13 and 14) and the system is parameterized by $n+2$ variables $\theta_0, \theta_1, \dots, \theta_{n+1}$. The total potential energy (12) for the rod is approximated by its discrete counterpart

$$V_{\text{dis}} = \frac{EI}{2} \sum_{i=1}^n \left(\frac{\theta_i - \theta_{i-1}}{ds} - \kappa_0 \right)^2 ds + \rho g (\ell - s_0) \sin(\theta_0) \frac{ds}{2} + \sum_{i=1}^{n-1} \rho g (\ell - s_i) \sin(\theta_i) ds + \rho g (\ell - s_n) \sin(\theta_n) \frac{ds}{2}. \quad (31)$$

The isoperimetric constraints (16)_{3,4} are also discretized and we need to impose boundary conditions on θ_i

$$\sin(\theta_0) \frac{ds}{2} + \sum_{i=1}^{n-1} \sin(\theta_i) ds + \sin(\theta_n) \frac{ds}{2} = h,$$

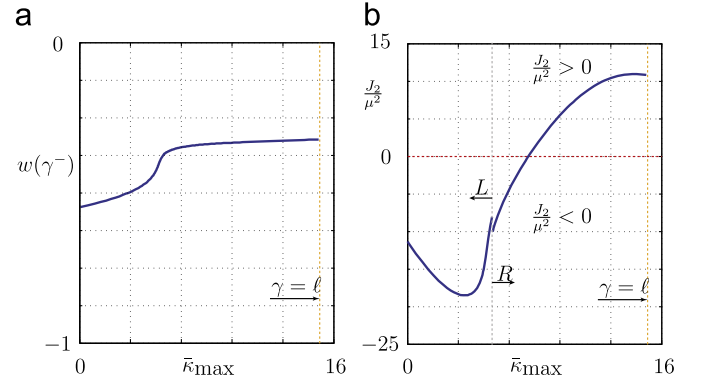


Fig. 15. Verification of the stability of the equilibrium in Fig. 10 with $W_{\text{ad}} = \frac{\omega}{\rho g \ell} = 3.2$, $D = \frac{EI}{\rho g \ell^3} = 0.1$, $M = \frac{m}{\rho \ell} = 2$, $\mu_k = 0.2$ and $\bar{\kappa}_{\max}$ ranging from 0 to 15. (a) The value $w(\gamma^-)$ of the solution $w(s)$ to the Riccati equation (44). (b) Stability ($J_2 > 0$) and instability ($J_2 < 0$) at the singular point $s = \gamma$ predicted by J_2 in (46).

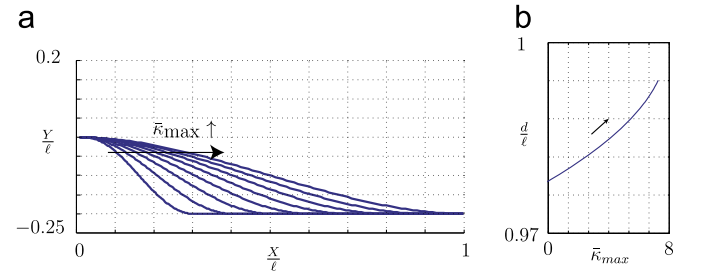


Fig. 16. Illustration of the locomotion during Phase C of the model system shown in Fig. 3 with a constant intrinsic curvature profile κ_0 (47) with $W_{\text{ad}} = 3.2$, $D = \frac{EI}{\rho g \ell^3} = 0.1$, $\mu_k = 0.2$, $M = 2$, and $\bar{\kappa}_{\max}$ ranging from 0 to 7.2. (a) The shape of the rod as $\bar{\kappa}_{\max}$ varies. (b) The dimensionless length of the soft limb in the E_1 direction $\frac{d}{\ell}$.

$$\cos(\theta_0) \frac{ds}{2} + \sum_{i=1}^{n-1} \cos(\theta_i) ds + \cos(\theta_n) \frac{ds}{2} = d, \quad \theta_0 = 0, \quad \frac{\theta_{n+1} - \theta_{n-1}}{2ds} = \kappa_0(\ell). \quad (32)$$

Note that the variable θ_{n+1} is a well-known device to enable the moment-free boundary condition at $s = \ell$ to the imposed and, later, to approximate $\theta(s = \ell)$.

The conditions (32)₃ can be directly imposed on (31) to reduce the dimension of the discretized system. That is,

$$V_{\text{dis}} = \frac{EI}{2} \sum_{i=1}^n \left(\frac{\theta_i - \theta_{i-1}}{ds} - \kappa_0 \right)^2 ds + \sum_{i=1}^{n-1} \rho g (\ell - s_i) \sin(\theta_i) ds + \rho g (\ell - s_n) \sin(\theta_n) \frac{ds}{2}, \quad (33)$$

and the discretized isoperimetric simplify to the pair of constraint functions c_1 and c_2

$$c_1 = \sum_{i=1}^{n-1} \sin(\theta_i) ds + \sin(\theta_n) \frac{ds}{2} - h, \quad c_2 = \frac{ds}{2} + \sum_{i=1}^{n-1} \cos(\theta_i) ds + \cos(\theta_n) \frac{ds}{2} - d. \quad (34)$$

We observe that this pair of functions depends on the states $\theta_1, \dots, \theta_n$.

We next seek minimizers of V_{dis} which satisfy two discretized constraints (34). The extremizer, which can be found in a standard manner using the method of Lagrange multipliers, is denoted by $(\theta_1^*, \dots, \theta_n^*)$. To examine the stability of the equilibrium state, it is

convenient to define three $(n \times n)$ matrices

$$\begin{aligned} F &= \nabla^2 V_{\text{dis}}(\theta_1^*, \dots, \theta_n^*), \\ H_1 &= \nabla^2 c_1(\theta_1^*, \dots, \theta_n^*), \quad H_2 = \nabla^2 c_2(\theta_1^*, \dots, \theta_n^*), \\ L &= F + \chi_1 H_1 + \chi_2 H_2. \end{aligned} \quad (35)$$

Here, the Lagrange multipliers χ_1 and χ_2 correspond to contributions from the normal force $\chi_1 \mathbf{E}_2$ and the static friction force $\chi_2 \mathbf{E}_1$. It is well known that for an equilibrium to be stable, the potential energy has to be locally minimized. To check whether the equilibrium $(\theta_1^*, \dots, \theta_n^*)$ locally minimizes Eq. (33), we use the classical method of checking the eigenvalues of L corresponding to the eigenvectors that lie in the $(n-2)$ -dimensional tangent subspace \mathcal{M} that is orthogonal to the (n) -dimensional gradient vectors $\nabla c_1 \in \mathbb{R}^n$ and $\nabla c_2 \in \mathbb{R}^n$ defined by the two discretized constraints (34). That is,

$$\mathcal{M} = \{u \in \mathbb{R}^n : \nabla c_1(\theta_1^*, \dots, \theta_n^*) \cdot u = 0 \text{ and } \nabla c_2(\theta_1^*, \dots, \theta_n^*) \cdot u = 0\}. \quad (36)$$

It should be clear that ∇c_1 and ∇c_2 are both n -dimensional arrays: $\nabla c_1 \in \mathbb{R}^n$ and $\nabla c_2 \in \mathbb{R}^n$. We denote an orthogonal basis for \mathcal{M} by the set of n -dimensional vectors $\{u_1, \dots, u_{n-2}\}$. This basis can be used to define a projection operator E where $Ez \in \mathcal{M}$ for all $z \in \mathbb{R}^n$

$$E = [u_1, \dots, u_{n-2}]. \quad (37)$$

With the help of E , the stability of the equilibrium can be established by showing that the smallest eigenvalue of $E^T L E$ is strictly positive [32]. As indicated by the results shown in Fig. 14, the quasistatic equilibrium configurations for State I satisfy the stability criterion.

With friction treated as a constant force, the discretized potential energy function reduces to

$$\begin{aligned} V_{\text{dis}} &= \frac{EI}{2} \sum_{i=1}^n \left(\frac{\theta_i - \theta_{i-1}}{ds} - \kappa_0 \right)^2 ds \\ &\quad + \rho g(\ell - s_0) \sin(\theta_0) \frac{ds}{2} + \sum_{i=1}^{n-1} \rho g(\ell - s_i) \sin(\theta_i) ds \\ &\quad + \rho g(\ell - s_n) \sin(\theta_n) \frac{ds}{2} \\ &\quad - F_f \cos(\theta_0) \frac{ds}{2} - F_f \sum_{i=1}^{n-1} \cos(\theta_i) ds - F_f \cos(\theta_n) \frac{ds}{2}, \end{aligned} \quad (38)$$

subject to the following conditions:

$$\begin{aligned} \sin(\theta_0) \frac{ds}{2} + \sum_{i=1}^{n-1} \sin(\theta_i) ds + \sin(\theta_n) \frac{ds}{2} &= h, \\ \theta_0 &= 0, \quad \frac{\theta_{n+1} - \theta_{n-1}}{2ds} = \kappa_0(\ell). \end{aligned} \quad (39)$$

We now follow the same procedure as we did for the first case, but with only a single constraint function. Our numerical results can be seen in Fig. 14 and we conclude that the quasi-static equilibrium configuration for State I satisfies the stability criterion.

4.2. Stability analysis for State II

For State II, we approximate the geometric constraints simply by replacing them with the constraint forces and then use the recent stability criteria from [27,28] for adhered intrinsically curved rods. Before deriving the stability criteria for the State II, we define the following pair of functions:

$$\begin{aligned} P &= -\rho g(\gamma - s) \sin(\theta) + n_1(\gamma) \cos(\theta) + n_2(\gamma) \sin(\theta), \\ P_1 &= \rho g(\gamma - s) \cos(\theta) - n_2(\gamma) \cos(\theta) + n_1(\gamma) \sin(\theta). \end{aligned} \quad (40)$$

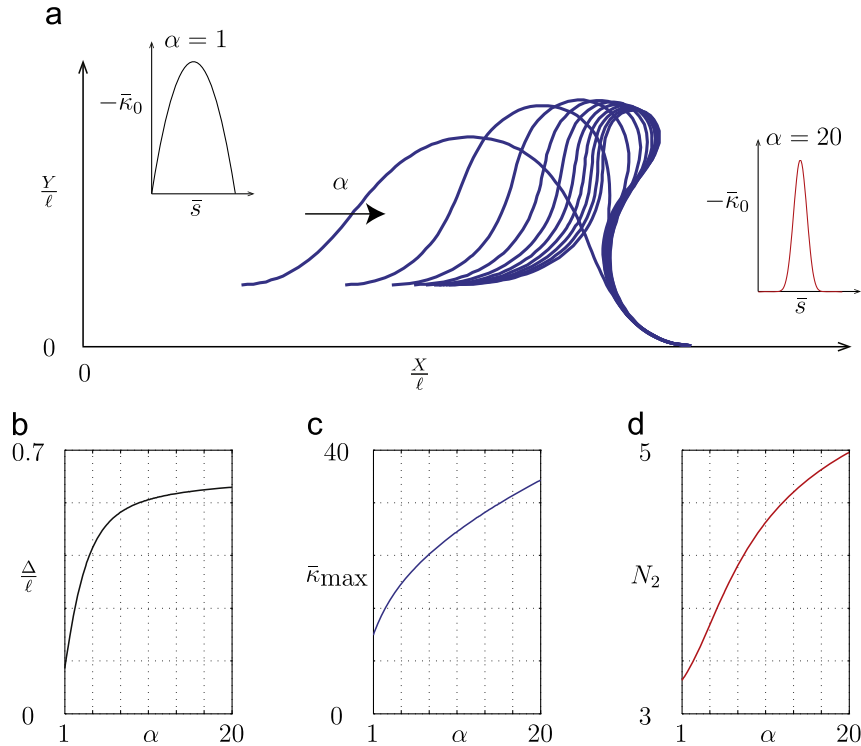


Fig. 17. Illustration of the effect of the degree of concentration of the intrinsic curvature profile on the locomotion. (a) The shape of the soft limb at $\gamma = \ell$ with $\alpha = \beta$ varying from 1 to 20. (b) The locomotion Δ/ℓ induced per period with $\alpha = \beta$ varying from 1 to 20. (c) The maximum intrinsic curvature $\bar{\kappa}_{\max}$ needed to get the soft limb detached with $\alpha = \beta$ varying from 1 to 20. (d) The normal force N_2 on the singular mass with $\alpha = \beta$ varying. The dimensionless parameters for this model are $W_{\text{ad}} = \frac{\omega}{\rho g \ell} = 3.2$, $M = \frac{m}{\rho \ell} = 2$, $D = \frac{EI}{\rho g \ell^3} = 0.1$, and $\mu_k = 0.2$.

To establish the criteria for stability for the solution $\theta = \theta^*$, we compute the second variation J of the potential energy function V in (23). Omitting details as they can easily be deduced from [27,28], we find that

$$J = \int_0^\gamma (El\eta'\eta' + P\eta^2) ds - 2 \left[\left[El(\theta^{*-} - \kappa_0)\eta' + P_1\eta \right]_\gamma \mu - \left[\left[El(\theta^{*-} - \kappa_0)(\theta^{*-} - \kappa_0) + P_1\theta^{*-} - \rho g \sin(\theta) \right]_\gamma \mu^2 \right]. \quad (41)$$

Here, $\eta = \eta(s)$ correspond to the variation in θ and μ corresponds to the variation in γ . These variations are subject to the following compatibility conditions:

$$\mu\theta^{*-}(\gamma^-) + \eta(\gamma^-) = 0, \quad \mu\theta^{*-}(\gamma^-) + 2\eta'(\gamma^-) = 0, \quad (42)$$

which we use to rewrite (41) as

$$J = \int_0^\gamma (El\eta'\eta' + P\eta^2) ds - \left(P_1\theta^{*-}(\gamma^-) + \kappa_0 P_1 + \rho g \sin(\theta(\gamma^-)) \right) \mu^2. \quad (43)$$

Following Legendre's classical method, if we can find a function $w(s)$ which satisfies the following Riccati equation:

$$\frac{\partial w}{\partial s} + P - \frac{w^2}{El} = 0, \quad w(0) = 0, \quad (44)$$

then J can be expressed as

$$J = \int_0^\gamma El \left(\eta' + \frac{w}{El} \eta \right)^2 ds + J_2, \quad (45)$$

where

$$\begin{aligned} J_2 &= - \left(P_1\theta^{*-}(\gamma^-) + \kappa_0 P_1 + \rho g \sin(\theta(\gamma^-)) \right) \mu^2 \\ &\quad + \eta^2(0)w(0) - \eta^2(\gamma^-)w(\gamma^-) \\ &= -\mu^2 \left(\theta^{*-}(\gamma^-)(\theta^{*-} w(\gamma^-) + P_1) + \kappa_0 P_1 \right). \end{aligned} \quad (46)$$

In arriving at the final expression for J_2 , we used the boundary conditions $\eta(0) = 0$ and $\eta(\gamma^-) = 0$. The function J_2 and the Riccati equation (44) form the basis for the stability criteria in [27,28]. If a bounded solution to (44) on $s \in [0, \gamma]$, and $J_2 \geq 0$, then the equilibrium configuration of the rod described by $\theta^*(s)$ satisfies a necessary condition for stability.

The condition on the solution w to the Riccati equation (44) feature in works examining buckling of the elastica (see e.g., [27,28,33] and references therein). Positivity of J_2 can be considered as a stability criterion for the adhesion at the point $s = \gamma$. As shown in Fig. 15, we are able to use the aforementioned criterion to show that the equilibrium configurations in Fig. 10 are stable. The results shown in Fig. 15(a) indicate that $w(s)$ is bounded, while the results in Fig. 15(b) show that the adhesion at $s = \gamma$ is stable when $\bar{\kappa}_{\max} > 7.65$.

5. The role of the curvature profile

From the previous sections, it is obvious that the key in inducing effective locomotion lies in the peeling process arising in Phase C. Given the soft robot technologies available to produce changes in the curvature profile $\kappa_0(s)$, such as pneumatic actuators and shape memory alloys [2,4,5,1], it is of interest to explore the effectiveness of given curvature profiles.

A naive proposed curvature profile would be a constant

$$\bar{\kappa}_0 = -\bar{\kappa}_{\max} \quad (47)$$

throughout the soft limb. We examined the locomotion that would be produced by such a curvature profile and the results are shown in Fig. 16. We found that instead of having $\frac{d}{\ell}$ decreasing, where d is the horizontal extent of the rod (cf. Fig. 6), as the detaching process begins (as in Fig. 10), $\frac{d}{\ell}$ increases by a small amount. This result predicts that as the intrinsic curvature is altered the soft limb would detach and adhere repeatedly without inducing any

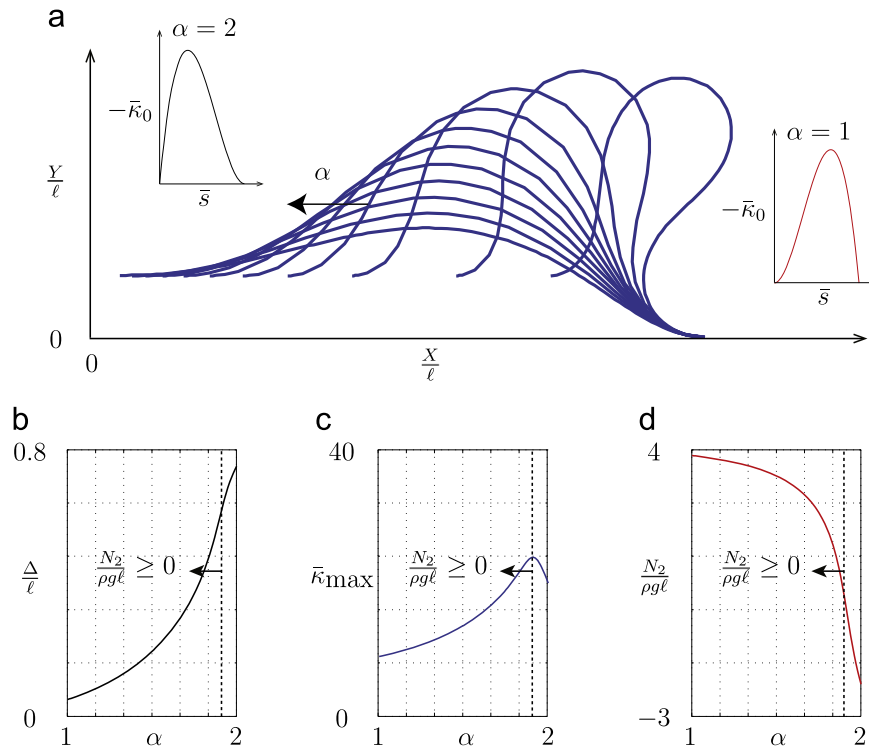


Fig. 18. Illustration of the effect of the degree of concentration of intrinsic curvature profile on the locomotion. (a) The shape of the soft limb at $\gamma = \ell$ with $\alpha = 3 - \beta$ varying from 1 to 2. (b) The locomotion $\frac{d}{\ell}$ induced per period with $\alpha = 3 - \beta$ varying from 1 to 2. (c) The maximum intrinsic curvature $\bar{\kappa}_{\max}$ needed to get the soft limb detached with $\alpha = 3 - \beta$ varying from 1 to 2. (d) The normal force $\frac{N_2}{\rho g \ell}$ on the mass m with $\alpha = 3 - \beta$ varying from 1 to 2. The dimensionless parameters for this model are $W_{\text{ad}} = \frac{w}{\rho g \ell} = 3.2$, $M = \frac{m}{\rho \ell} = 2$, $D = \frac{EI}{\rho g \ell^3} = 0.1$, and $\mu_k = 0.2$.

effective displacement of the mass m . In conclusion, the profile (47) is not effective.

One of the conclusions that can be drawn from Fig. 16 is the potential need to concentrate the curvature variation along the rod. To see that this is indeed the case, we consider more complex forms of (28)

$$\bar{\kappa}_0(\bar{s}) = -\bar{\kappa}_{\max} \frac{(\alpha + \beta)^{(\alpha + \beta)\bar{s}^\beta} (1 - \bar{s})^\alpha}{\alpha^\alpha \beta^\beta}. \quad (48)$$

where α and β are positive constants. The maximal value $|\bar{\kappa}_0(\bar{s})|$ occurs when $\bar{s} = \frac{\beta}{\alpha + \beta}$

$$\bar{\kappa}_0\left(\bar{s} = \frac{\beta}{\alpha + \beta}\right) = -\bar{\kappa}_{\max}. \quad (49)$$

From Fig. 17, we can find that the net motion $\frac{\Delta}{\ell}$ of the mass m improves significantly as α increases from 1 to 5. However, the maximum curvature $\bar{\kappa}_{\max}$ needed to completely detach the soft limb also increases. In the regime where α increases from 5 to 20, the maximum curvature $\bar{\kappa}_{\max}$ increases with a relatively small improvement in the value of $\frac{\Delta}{\ell}$ and the normal force $\frac{N_2}{\rho g \ell}$ on the mass m is always positive.

After investigating the effects of the distribution of curvature, the next feature of interest is the location where the curvature is largest. It can be easily shown from (48) that the location where the curvature is maximum occurs at $\bar{s} = \frac{\beta}{\alpha + \beta}$. The larger the value of α , the closer the location of the maximum is to the mass m . To make different intrinsic curvature profiles comparable, we set $\alpha + \beta = \text{const}$. As can be seen from Fig. 18, we find that as α was increased, the locomotion $\frac{\Delta}{\ell}$ improved significantly at a cost of moderately increasing the maximum curvature $\bar{\kappa}_{\max}$. However, the normal force $\frac{N_2}{\rho g \ell}$ became negative when α exceeded 1.9 and m would have lifted off the surface.

5.1. Effects of varying mass m

We have assumed throughout our analysis that the mass m is fixed. It is clearly of interest to examine how the locomotion scheme will be effected by changing the mass m . The two features we will focus on are the displacement Δ achieved in one cycle and the maximum intrinsic curvature $\bar{\kappa}_{\max}$ needed to achieve detachment the rod at the end of Phase C of the locomotion scheme. A summary of our

results is shown in Fig. 19, as the mass parameter $M = \frac{m}{\rho \ell}$ increases, we find that the net displacement decreases slightly. However, the maximum curvature $\bar{\kappa}_{\max}$ needed to produce a locomotion of locomotion such as that shown in Fig. 19 will increase significantly.

6. Conclusions

Based on the numerical simulations and analysis of the simple model, the following conclusions on locomotion can be drawn:

1. In this locomotion scheme, controlling the magnitude of the curvature is sufficient to enable the soft limb to overcome static friction at the tip contact.
2. The detachment of the soft limb at the end of the adhesion phase of the motion is the key process to induce locomotion.
3. Concentration of curvature is crucial to enabling locomotion and it is more effective to place the concentration towards the mass rather than the tip.

These observations have potential influence on how soft robots are operated and designed. The design and operation of these devices include the actuator technology, materials, and geometric dimensions required to deliver an effective locomotion. Such insights have particularly important implications in the design and operation of soft robots. In addition, most of the results presented in this paper can be adopted to study peristaltic locomotion.

Acknowledgments

Support from a Defense Advanced Research Projects (DARPA) 2012 Young Faculty Award to Carmel Majidi is gratefully acknowledged. Xuance Zhou is grateful for the support of an Anselmo Macchi Fellowship for Engineering Graduate Students and a J.K. Zee Fellowship.

References

- [1] R.F. Shepherd, F. Ilievski, W. Choi, S.A. Morin, A.A. Stokes, A.D. Mazzeo, X. Chen, M. Wang, G.M. Whitesides, Multigait soft robots, *Proc. Natl. Acad. Sci. USA* 108 (51) (2011) 20400–20403. <http://dx.doi.org/10.1073/pnas.1116564108>.
- [2] C. Laschi, M. Cianchetti, Soft robotics: new perspectives for robot body and control, *Front. Bioeng. Biotechnol.* 2 (3), 2014, <http://dx.doi.org/10.3389/fbioe.2014.00003>.
- [3] C. Onal, D. Rus, Autonomous undulatory serpentine locomotion utilizing body dynamics of a fluidic soft robot, *Bioinspir. Biomimet.* 8 (2) (2013) 026003. <http://dx.doi.org/10.1088/1748-3182/8/2/026003>.
- [4] J. Lee, R.S. Fearing, K. Komvopoulos, Directional adhesion of gecko-inspired angled microfiber arrays, *Appl. Phys. Lett.* 93 (19) (2008) 191910. <http://dx.doi.org/10.1063/1.3006334>.
- [5] C. Majidi, Soft robotics: a perspective—current trends and prospects for the future, *Soft Robot.* 1 (P) (2013) 5–11. <http://dx.doi.org/10.1089/soro.2013.000>.
- [6] C. Majidi, R.F. Shepherd, R. Kramer, G.M. Whitesides, R.J. Wood, Influence of surface traction on soft robot undulation, *Int. J. Robot. Res.* 32 (13) (2013) 1577–1584. <http://dx.doi.org/10.1177/0278364913498432>.
- [7] Y. Nakazato, Y. Sonobe, S. Toyama, Development of an in-pipe micro mobile robot using peristalsis motion, *J. Mech. Sci. Technol.* 24 (1) (2010) 51–54. <http://dx.doi.org/10.1007/s12206-009-1174-x>.
- [8] S. Seok, C. Onal, R.J. Wood, D. Rus, S. Kim, Meshworm: a peristaltic soft robot with antagonistic nickel titanium coil actuators, *IEEE/ASME Trans. Mechatron.* 18 (5) (2013) 1485–1497. <http://dx.doi.org/10.1109/TMECH.2012.2204070>.
- [9] R.J. Webster, B.A. Jones, Design and kinematic modeling of constant curvature continuum robots: a review, *Int. J. Robot. Res.* 29 (3) (2010) 1661–1683. <http://dx.doi.org/10.1177/0278364910368147>.
- [10] X. Zhou, C. Majidi, O.M. O'Reilly, Energy efficiency in friction-based locomotion mechanisms for soft and hard robots: slower can be faster, *Nonlinear Dyn.* 78 (4) (2015) 2811–2821. <http://dx.doi.org/10.1007/s11071-014-1627-3>.
- [11] Z. Nagy, D. Frutiger, R. Leine, C. Glocker, B. Nelson, Modeling and analysis of wireless resonant magnetic microactuators, in: 2010 IEEE International Conference on Robotics and Automation (ICRA), 2010, pp. 1598–1603. <http://dx.doi.org/10.1109/ROBOT.2010.5509260>.

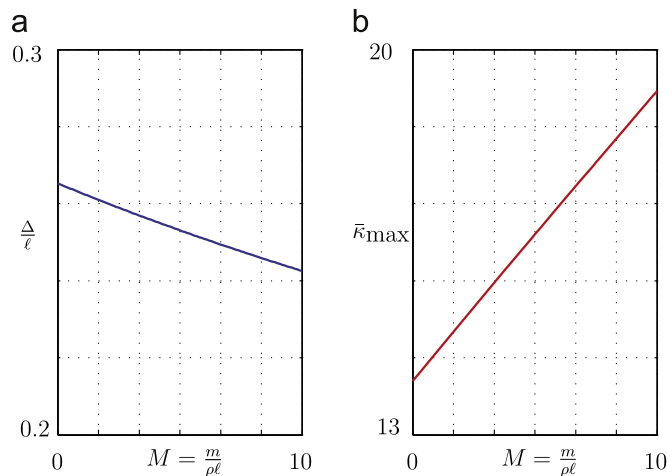


Fig. 19. Illustration of the effect of the mass parameter $M = \frac{m}{\rho \ell}$ on the locomotion. (a) The net locomotion $\frac{\Delta}{\ell}$ induced per cycle as a function of M . (b) The maximum intrinsic curvature $\bar{\kappa}_{\max}$ needed to detach the rod at the end of Phase C of the locomotion scheme as a function of M . The dimensionless parameters for this model are $W_{\text{ad}} = \frac{w}{\rho g \ell} = 3.2$, $D = \frac{EI}{\rho g \ell^3} = 0.1$, and $\mu_k = 0.2$.

- [12] Z. Nagy, R. Leine, D. Frutiger, C. Glocker, B. Nelson, Modeling the motion of microrobots on surfaces using nonsmooth multibody dynamics, *IEEE Trans. Robot.* 28 (5) (2012) 1058–1068. <http://dx.doi.org/10.1109/TRO.2012.2199010>.
- [13] R. Murthy, A. Das, D.O. Popa, ARRLpede: a stick-slip micro crawler/conveyor robot constructed via 2 1/2D MEMS assembly, in: *IEEE/RSJ International Conference on Intelligent Robots and Systems*, 2008. IROS 2008, 2008, pp. 34–40. <http://dx.doi.org/10.1109/IROS.2008.4651181>.
- [14] R. Murthy, A. Das, D.O. Popa, H.E. Stephanou, ARRLpede: an assembled die-scale microcrawler, *Adv. Robot.* 25 (8) (2011) 965–990. <http://dx.doi.org/10.1163/016918611X568602>.
- [15] P. Gidoni, G. Noselli, A. DeSimone, Crawling on directional surfaces, *Int. J. Non-Linear Mech.* 61 (2014) 65–73. <http://dx.doi.org/10.1016/j.ijnonlinmec.2014.01.012>.
- [16] G. Noselli, A. DeSimone, A robotic crawler exploiting directional frictional interactions: experiments, numerics and derivation of a reduced model, *Proc. R. Soc. Lond. A: Math. Phys. Eng. Sci.* 470 (2171) (2014) 20140333. <http://dx.doi.org/10.1098/rspa.2014.0333>.
- [17] C. Pawashe, S. Floyd, M. Sitti, Modeling and experimental characterization of an untethered magnetic micro-robot, *Int. J. Robot. Res.* 28 (8) (2009) 1077–1094. <http://dx.doi.org/10.1177/0278364909341413>.
- [18] H.Y. Elder, Peristaltic mechanisms, in: H.Y. Elder, E.R. Trueman (Eds.), *Aspects of Animal Movement*, Society for Experimental Biology: Seminar Series, vol. 5, Cambridge University Press, Cambridge, UK, 1985, pp. 71–92.
- [19] R. McNeil Alexander, *Principles of Animal Locomotion*, Princeton University Press, Princeton, NJ, 2003.
- [20] Y. Tanaka, K. Ito, T. Nakagaki, R. Kobayashi, Mechanics of peristaltic locomotion and role of anchoring, *J. R. Soc. Interface* 9 (67) (2012) 222–233. <http://dx.doi.org/10.1098/rsif.2011.0339>.
- [21] M. Denny, The role of gastropod pedal mucus in locomotion, *Nature* 285 (1) (1980) 160–161. <http://dx.doi.org/10.1038/285160a0>.
- [22] K. Galloway, P. Polygerinos, C. Walsh, R. Wood, Mechanically programmable bend radius for fiber-reinforced soft actuators, in: *2013 16th International Conference on Advanced Robotics (ICAR)*, 2013, pp. 1–6. <http://dx.doi.org/10.1109/ICAR.2013.6766586>.
- [23] R. Shepherd, A. Stokes, J. Freake, J. Barber, P. Snyder, A. Mazzeo, L. Cademartiri, S. Morin, G. Whitesides, Using explosions to power a soft robot, *Angew. Chem. Int. Ed.* 52 (10) (2013) 2892–2896. <http://dx.doi.org/10.1002/anie.201209540>.
- [24] K. Suzumori, S. Endo, T. Kanda, N. Kato, H. Suzuki, A bending pneumatic rubber actuator realizing soft-bodied manta swimming robot, in: *2007 IEEE International Conference on Robotics and Automation*, 2007, pp. 4975–4980. <http://dx.doi.org/10.1109/ROBOT.2007.364246>.
- [25] K. Takashima, T. Noritsugu, J. Rossiter, S. Guo, T. Mukai, Development of curved type pneumatic artificial rubber muscle using shape-memory polymer, in: *2011 Proceedings of SICE Annual Conference (SICE)*, 2011, pp. 1691–1695.
- [26] S. Wakimoto, K. Ogura, K. Suzumori, Y. Nishioka, Miniature soft hand with curling rubber pneumatic actuators, in: *2009 IEEE International Conference on Robotics and Automation*, 2009, pp. 556–561. <http://dx.doi.org/10.1109/ROBOT.2009.5152259>.
- [27] C. Majidi, O.M. O'Reilly, J.A. Williams, On the stability of a rod adhering to a rigid surface: shear-induced stable adhesion and the instability of peeling, *J. Mech. Phys. Solids* 60 (5) (2012) 827–843. <http://dx.doi.org/10.1016/j.jmps.2012.01.015>.
- [28] C. Majidi, O.M. O'Reilly, J.A. Williams, Bifurcations and instability in the adhesion of intrinsically curved rods, *Mech. Res. Commun.* 49 (0) (2013) 13–16. <http://dx.doi.org/10.1016/j.mechrescom.2013.01.004>.
- [29] N.A. Faruk Senan, O.M. O'Reilly, T.N. Tresieras, Modeling the growth and branching of plants: a simple rod-based model, *J. Mech. Phys. Solids* 56 (10) (2008) 3021–3036. <http://dx.doi.org/10.1016/j.jmps.2008.06.005>.
- [30] O.M. O'Reilly, T.N. Tresieras, On the evolution of intrinsic curvature in rod-based models of growth in long slender plant stems, *Int. J. Solids Struct.* 48 (9) (2011) 1239–1247. <http://dx.doi.org/10.1016/j.ijsolstr.2010.12.006>.
- [31] Y. Farjoun, J. Neu, The tallest column: a dynamical system approach using a symmetry solution, *Stud. Appl. Math.* 115 (3) (2005) 319–337. <http://dx.doi.org/10.1111/j.1467-9590.2005.00316.x>.
- [32] D.G. Luenberger, Y. Ye, *Linear and Nonlinear Programming*, International Series in Operations Research & Management Science, 3rd ed., vol. 116, Springer, New York, 2008.
- [33] O.M. O'Reilly, D.M. Peters, Nonlinear stability criteria for tree-like structures composed of branched elastic rods, *Proc. R. Soc. A: Math. Phys. Eng. Sci.* 468 (2137) (2012) 206–226. <http://dx.doi.org/10.1098/rspa.2011.0291>.